Rotating non-Oberbeck–Boussinesq Rayleigh–Bénard convection in water

Horn, S. & Shishkina, O.

Original citation:
Horn, S & Shishkina, O 2014, 'Rotating non-Oberbeck–Boussinesq Rayleigh–Bénard convection in water' Physics of Fluids, vol. 26, no. 5, 055111.
https://dx.doi.org/10.1063/1.4878669

DOI 10.1063/1.4878669
ISSN 1070-6631
ESSN 1089-7666

Publisher: AIP Publishing

PHYSICS OF FLUIDS **26**, 055111 (2014)

Rotating non-Oberbeck–Boussinesq Rayleigh–Bénard convection in water

Susanne Horn[1,2,a)] and Olga Shishkina[1,2]
[1]*Max Planck Institute for Dynamics and Self-Organization, 37077 Göttingen, Germany*
[2]*Institute of Aerodynamics and Flow Technology, German Aerospace Center, 37073 Göttingen, Germany*

(Received 3 February 2014; accepted 7 May 2014; published online 28 May 2014)

Rotating Rayleigh–Bénard convection in water is studied in direct numerical simulations, where the temperature dependence of the viscosity, the thermal conductivity, and the density within the buoyancy term is taken into account. In all simulations, the arithmetic mean of the lowest and highest temperature in the system equals 40 °C, corresponding to a Prandtl number of $Pr = 4.38$. In the non-rotational case, the Rayleigh number Ra ranges from 10^7 to 1.16×10^9 and temperature differences Δ up to 70 K are considered, whereas in the rotational case the inverse Rossby number range from $0.07 \leq 1/Ro \leq 14.1$ is studied for $\Delta = 40$ K with the focus on $Ra = 10^8$. The non-Oberbeck–Boussinesq (NOB) effects in water are reflected in an up to 5.5 K enhancement of the center temperature and in an up to 5% reduction of the Nusselt number. The top thermal and viscous boundary layer thicknesses increase and the bottom ones decrease, while the sum of the corresponding top and bottom thicknesses remains as in the classical Oberbeck–Boussinesq (OB) case. Rotation applied to NOB thermal convection reduces the central temperature enhancement. Under NOB conditions the top (bottom) thermal and viscous boundary layers become equal for a slightly larger (smaller) inverse Rossby number than in the OB case. Furthermore, for rapid rotation the thermal bottom boundary layers become thicker than the top ones. The Nusselt number normalized by that in the non-rotating case depends similarly on $1/Ro$ in both, the NOB and the OB cases. The deviation between the Nusselt number under OB and NOB conditions is minimal when the thermal and viscous boundary layers are equal. [http://dx.doi.org/10.1063/1.4878669]

I. INTRODUCTION

Rayleigh–Bénard convection is one of the classical problems of fluid dynamics. Similar as Taylor–Couette or pipe flow, the setup is rather simple: It consists of a fluid confined between a heating plate at the bottom and a cooling plate at the top. For theoretical investigations it is usually convenient to have an infinite lateral extent, whereas in experiments elementary geometries such as cubes or cylinders are used. Numerical simulations have the advantage that both is easy to accomplish. Despite its simplicity, the occurring buoyancy driven flows are highly complex and we are still far away from a complete understanding. Thus, after being first described by Bénard[1] and Lord Rayleigh[2] it kept on being an active field of research for over a century now. Some recent reviews are available by Bodenschatz, Pesch, and Ahlers,[3] Ahlers, Grossmann, and Lohse,[4] Lohse and Xia,[5] Chillà and Schumacher,[6] and Stevens, Clercx, and Lohse[7] shedding light on different aspects.

The main reason for the ongoing interest is not only pure scientific curiosity but also the importance of convective processes in engineering, meteorology, geo-, and astrophysics. Examples are the ventilation of buildings and aircrafts, the flow in the atmosphere and oceans of planets,

a)susanne.horn@ds.mpg.de

including our Earth, and in the convective zone of stars. In the present paper, we want to examine two different aspects beyond the standard description of Rayleigh–Bénard convection which might help to get closer to the prediction of realistic flows: First, the influence of temperature-dependent material properties and second, the influence of rotation, both separately and in combination.

Commonly, variations of the fluid properties within the Rayleigh–Bénard cell are ignored due to their assumed smallness. Only the variability of the density is accounted for in the buoyancy force. As a result, the system exhibits a perfect top-bottom symmetry in a statistical sense. In nature and so to say in all experiments, one always encounters a break-up of this symmetry, since these idealized conditions can never be fulfilled exactly. These deviations are called non-Oberbeck-Boussinesq (NOB) effects.

NOB effects caused by the temperature-dependence of the material properties have been investigated for different fluids in non-rotating convection.[8–13] However, only few systematic studies can be found when rotation comes into play. If, then concerning pattern formation and, thus, with larger aspect ratios.[14] Our objective is to examine the flow in turbulent thermal convection of water considering its actual properties and the influence of rotation by means of three-dimensional direct numerical simulations (DNS).

II. NUMERICAL METHODOLOGY

A. Validity of the Oberbeck–Boussinesq approximation

In most numerical investigations of Rayleigh–Bénard convection, the Oberbeck–Boussinesq (OB) approximation[15,16] is employed. This means, that all material properties are constant, i.e., they do not vary with pressure or temperature and, consequently, the fluid is assumed to be incompressible. The only exception is the density in the buoyancy term, which varies linearly with temperature therein. Since this simplifies the governing equations tremendously and, thus, allows for making theoretical predictions, it is also desired in most of the experimental investigations to operate under OB conditions.

However, it is intuitively clear that if the height H of the Rayleigh–Bénard cell is too large or the temperature difference Δ between the heating and cooling plate is too big, then the material properties are non-uniform within the cell. Hence, the question is: When is the OB approximation valid? A mathematical rigorous answer to it was given by Gray and Giorgini.[17] By fixing the maximum residual error, the validity range of the OB approximation can be calculated explicitly within the requested accuracy.

In general, for liquids the pressure-dependence can be neglected and only the temperature-dependence is of importance. In the present work, we only consider water at an arithmetic mean temperature of $T_m = (T_t + T_b)/2 = 40\,^{\circ}\mathrm{C}$, where T_t is the temperature at the top and T_b is the temperature at the bottom. In the following the indices m, t, and b will always indicate that a quantity is given for T_m, T_t, and T_b, respectively. The deviation of the material properties from their values at T_m is shown in Fig. 1(a) in the range between $10\,^{\circ}\mathrm{C}$ and $70\,^{\circ}\mathrm{C}$. Their functional dependency was given by Ahlers *et al.*[10] in terms of polynomials of the temperature up to cubic order ($i = 3$) with certain prefactors a_i,

$$\frac{X - X_m}{X_m} = \sum_i a_i (T - T_m)^i \quad X \in \{\rho,\ \kappa,\ c_p,\ \nu,\ \alpha,\ \Lambda\}. \tag{1}$$

Here X stands for the various material properties, i.e., the density ρ, the heat diffusivity κ, the specific heat capacity c_p, the kinematic viscosity ν, the isobaric expansion coefficient α, and the heat conductivity Λ. Using these polynomial functions, we can calculate the validity range of the OB approximation for water similar as was done in Horn, Shishkina, and Wagner[8] for glycerol. By requiring a maximum residual error of 10% the two constraints are $H/\Delta < 35036\,\mathrm{cm/K}$ and $\Delta < 0.268\,\mathrm{K}$. The resulting diagram is visualized in Fig. 1(b). Hence, in most experiments in water the height of the Rayleigh–Bénard cell is not crucial, whereas the employed temperature difference is indeed due to the variation of the viscosity. However, experiments and 2D-simulations[10,13] have

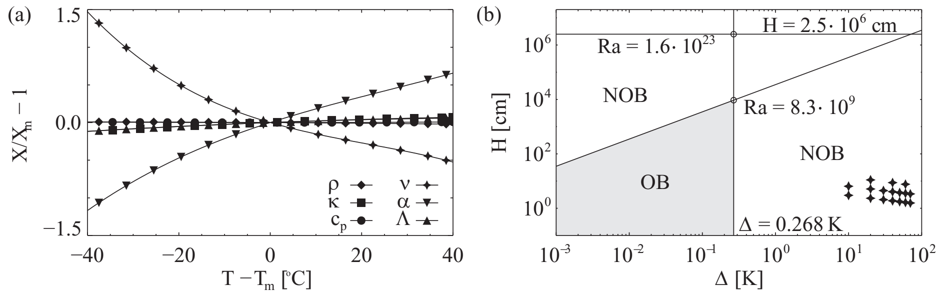

FIG. 1. (a) Relative deviation of the material properties X of water from their values X_m at a mean temperature of $T_m = 40\,^\circ$C, adopted from Ahlers *et al.*;[10] diamonds: density ρ, squares: thermal diffusivity κ, circles: specific heat capacity c_p, stars: kinematic viscosity ν, downward triangles: isobaric expansion coefficient α, upward triangle: heat conductivity Λ. (b) Diagram of the validity range of the OB approximation according to Gray and Giorgini.[17] The gray shaded area shows the parameter range where the OB approximation is valid within a residual error of 10%. The stars denote the NOB DNS data points.

shown that some quantities, as, for example, the Nusselt number Nu, remain almost unchanged under NOB conditions.

B. Parameter space and governing equations

The standard control parameters for rotating Rayleigh–Bénard convection are all defined for the mean temperature T_m, i.e., the Rayleigh, Prandtl, and Rossby number are given by

$$Ra = \frac{\alpha_m g \Delta H^3}{\kappa_m \nu_m}, \quad Pr = \frac{\nu_m}{\kappa_m}, \quad Ro = \frac{\sqrt{g\alpha_m H \Delta}}{2\Omega H}, \tag{2}$$

respectively, with Ω being the applied rotational speed and g the acceleration due to gravity. The Rossby number is an inverse dimensionless rotation rate. To avoid confusion, rather $1/Ro$ is used such that a large value of $1/Ro$ indicates rapid rotation. Furthermore, we introduce the Ekman number

$$Ek = \frac{\nu_m}{\Omega H^2} = 2Ro\,Pr^{1/2}Ra^{-1/2}, \tag{3}$$

since this has proven to be a convenient dimensionless number in the boundary layer analysis of rotating flows,[18] sometimes defined with an extra factor of one half.[19,20]

The simulations without rotation were performed under OB and various NOB conditions for the Rayleigh numbers 10^7, 10^8, 10^9, and 1.16×10^9. The Prandtl number is set to $Pr = 4.38$. The diameter-to-height aspect ratio is $\Gamma = D/H = 1$ or, equivalently, the radius-to-height aspect ratio is $\gamma = R/H = 1/2$. Because we are interested in strong NOB effects, we chose temperature differences up to 70 K, however, in a temperature range far enough away from the water density anomaly at around $4\,^\circ$C. Furthermore, we only consider the temperature dependence of the conductivity Λ, the viscosity ν, and the variation of the density ρ within the buoyancy term. This approach is accurate for most liquids and allows to predict the most important NOB effects.[8,9] It should also be noted that by specifying Δ and the temperature-dependencies of the material properties, one also fixes all the other dimensions in the NOB simulations for a constant Ra. The parameters for the performed DNS in the non-rotating case are presented in Fig. 1(b) and in Table I.

For the simulations with rotation, we set the temperature difference to $\Delta = 40$ K and the Rayleigh number to $Ra = 10^8$ in the NOB case. The inverse Rossby number range is given by $1/Ro \in \{0.07, 0.24, 0.35, 0.71, 1.01, 1.41, 2.36, 2.83, 3.54, 4.71, 7.07, 11.31, 14.14\}$. Hence, the smallest Ekman number we achieve is $Ek \approx 3 \times 10^5$, thus, still about one magnitude larger than when asymptotically reduced equations are to be expected to be sufficient, as introduced by Julien *et al.*[20] In the OB case, additionally to $Ra = 10^8$, moreover a series of DNS was conducted for $Ra = 1.16 \times 10^9$ and $1/Ro \in \{0.24, 0.71, 1.41, 2.36, 3.54, 7.07, 11.31, 14.14\}$ to compare with available experimental data by Kunnen *et al.*[21] with exactly the same Prandtl number of $Pr = 4.38$.

TABLE I. Simulation parameters, i.e., Rayleigh number Ra, temperature difference Δ, height H and the grid resolution in radial, azimuthal, and vertical direction $N_r \times N_\phi \times N_z$ of the non-rotating DNS. The OB simulations are dimensionless, while NOB simulations always imply dimensions.

Case	Ra	Δ(K)	H(cm)	$N_r \times N_\phi \times N_z$
OB	10^7	...	...	$64 \times 512 \times 128$
NOB	10^7	$\{10, 20, 30, 40, 50, 60, 70\}$	$\{3.0, 2.3, 2.1, 1.9, 1.8, 1.6, 1.6\}$	$64 \times 512 \times 128$
OB	10^8	...	...	$192 \times 512 \times 384$
NOB	10^8	$\{10, 20, 30, 40, 50, 60, 70\}$	$\{6.5, 5.1, 4.5, 4.1, 3.8, 3.6, 3.4\}$	$192 \times 512 \times 384$
OB	10^9	...	...	$384 \times 512 \times 768$
NOB	10^9	$\{20, 40, 60\}$	$\{11.0, 8.8, 7.7\}$	$384 \times 512 \times 768$
OB	1.16×10^9	...	...	$384 \times 512 \times 768$

Since the dimensions are fixed under NOB conditions, it is also possible to estimate the potential importance of centrifugal buoyancy effects by calculating the Froude number,

$$Fr = \frac{\Omega^2 D}{2g} = \frac{\alpha_m \Delta \Gamma}{8 Ro^2}. \tag{4}$$

In experiments, it is usually attempted to keep Fr as small as possible, i.e., around 0.05 and lower.[22] For our fastest rotation rates, i.e., $1/Ro = 14.14$, and $\Delta = 40\,\mathrm{K}$ the Froude number is $Fr = 0.4$ which suggests that centrifugal buoyancy effects might be observed[23–27] and only for $1/Ro \lesssim 5$ they are expected to be negligible. Considering $Fr \neq 0$, however, would lead to an additional source of breaking the symmetry about the mid plane and it would be hard to decouple centrifugal buoyancy and NOB effects. Thus, we deliberately set $Fr \equiv 0$.

Hence, rotating Rayleigh–Bénard convection in water is well-defined by the following set of equations, given in cylindrical coordinates (r, ϕ, z): the continuity equation

$$\frac{1}{r}\partial_r (r u_r) + \frac{1}{r}\partial_\phi u_\phi + \partial_z u_z = 0, \tag{5}$$

the Navier–Stokes equations in the co-rotating frame of reference

$$\begin{aligned}
D_t u_r - \frac{u_\phi^2}{r} + \frac{1}{\rho_m}\partial_r p &= \frac{1}{r}\partial_r (r \nu \tau_{rr}) + \frac{1}{r}\partial_\phi \left(\nu \tau_{r\phi}\right) + \partial_z (\nu \tau_{rz}) - \frac{1}{r}\nu \tau_{\phi\phi} - 2\Omega u_\phi, \\
D_t u_\phi + \frac{u_r u_\phi}{r} + \frac{1}{\rho_m}\frac{1}{r}\partial_\phi p &= \frac{1}{r^2}\partial_r \left(r^2 \nu \tau_{\phi r}\right) + \frac{1}{r}\partial_\phi \left(\nu \tau_{\phi\phi}\right) + \partial_z \left(\nu \tau_{\phi z}\right) + 2\Omega u_r, \\
D_t u_z + \frac{1}{\rho_m}\partial_z p &= \frac{1}{r}\partial_r (r \nu \tau_{zr}) + \frac{1}{r}\partial_\phi \left(\nu \tau_{z\phi}\right) + \partial_z (\nu \tau_{zz}) + \frac{\rho_m - \rho}{\rho_m} g,
\end{aligned} \tag{6}$$

and the temperature equation

$$\rho_m c_{p,m} D_t T = \frac{1}{r}\partial_r (\Lambda r \partial_r T) + \frac{1}{r^2}\partial_\phi (\Lambda \partial_\phi T) + \partial_z (\Lambda \partial_z T). \tag{7}$$

Here, D_t is the material derivative

$$D_t = \partial_t + u_r \partial_r + \frac{1}{r} u_\phi \partial_\phi + u_z \partial z, \tag{8}$$

p denotes the pressure, u_r, u_ϕ, and u_z are the radial, azimuthal, and vertical velocity components, respectively, and the tensor τ is defined as

$$\begin{aligned}
\tau_{rr} &= 2\partial_r u_r, & \tau_{r\phi} = \tau_{\phi r} &= \tfrac{1}{r}\partial_\phi u_r + \partial_r u_\phi - \tfrac{u_\phi}{r}, \\
\tau_{\phi\phi} &= 2\left(\tfrac{1}{r}\partial_\phi u_\phi + \tfrac{u_r}{r}\right), & \tau_{\phi z} = \tau_{z\phi} &= \partial_z u_\phi + \tfrac{1}{r}\partial_\phi u_z, \\
\tau_{zz} &= 2\partial_z u_z, & \tau_{zr} = \tau_{rz} &= \partial_z u_r + \partial_r u_z.
\end{aligned} \tag{9}$$

TABLE II. Nusselt numbers as presented in Fig. 13 for the OB and the NOB case with $\Delta = 40$ K and $Ra = 10^8$. Furthermore, the last column shows the deviation of the centre temperature from the mean temperature for this NOB case as presented in Fig. 8(b).

$1/Ro$	Nu_{OB}	Nu_{NOB}	$T_c - T_m$(K)
0.0	32.94 ± 0.10	32.31 ± 0.08	1.80 ± 0.12
0.07	32.85 ± 0.15	32.21 ± 0.14	1.76 ± 0.10
0.24	32.92 ± 0.13	32.52 ± 0.42	1.80 ± 0.10
0.35	32.97 ± 0.21	32.24 ± 0.13	1.75 ± 0.14
0.71	34.05 ± 0.19	34.07 ± 0.22	1.72 ± 0.11
1.01	35.18 ± 0.21	34.55 ± 0.03	1.75 ± 0.11
1.41	35.26 ± 0.07	35.46 ± 0.76	1.70 ± 0.11
2.36	36.77 ± 0.06	35.86 ± 0.16	1.76 ± 0.12
2.83	37.01 ± 0.07	36.29 ± 0.08	1.75 ± 0.12
3.54	37.62 ± 0.06	37.35 ± 0.46	1.57 ± 0.04
4.71	38.51 ± 0.18	38.43 ± 0.13	1.54 ± 0.13
7.07	38.60 ± 0.14	38.57 ± 0.33	1.21 ± 0.09
11.31	34.53 ± 0.40	32.86 ± 0.44	0.93 ± 0.08
14.14	29.81 ± 0.37	28.63 ± 0.63	0.60 ± 0.04

C. Numerical procedure

To simulate rotating turbulent Rayleigh–Bénard convection the governing equations (5)–(7) are made dimensionless by using the radius R, the buoyancy velocity $\sqrt{g\alpha_m R\Delta}$, the temperature difference Δ, and the value of the material properties at the mean temperature T_m, i.e., ν_m, Λ_m, ρ_m, as reference scales. This also yields a reference time $R/\sqrt{g\alpha_m R\Delta}$ and a reference pressure $\rho_m g\alpha_m R\Delta$. The resulting equations are solved in discretized form using a finite volume code for cylindrical domains.

The code uses a fourth-order accurate spatial discretization scheme and a hybrid explicit/semi-implicit Leapfrog-Euler time integration scheme. More details about the OB version of the code can be found in Shishkina and Wagner.[28] For details on the implementation of temperature-dependent material properties and the Coriolis term we refer to Horn, Shishkina, and Wagner[8] and Horn and Shishkina.[29] The lateral wall is adiabatic and the heating and cooling plates are isothermal; the dimensionless top temperature is set to $\hat{T}_t = -0.5$ and the bottom temperature is set to $\hat{T}_b = 0.5$. Here the hat denotes dimensionless quantities, but it will be dropped for clarity in the following. For all walls no-slip boundary conditions for the velocity are imposed. All boundary conditions are completed by setting a 2π periodicity in azimuthal direction.

The computational meshes are staggered and their nodes are distributed equidistantly in azimuthal direction and non-equidistantly in vertical and radial direction, i.e., the nodes are clustered close to the walls. The numerical resolution was chosen in such a way that the resolution requirements by Shishkina *et al.*[30] are fulfilled. It can be found in Table I. However, at least twice as many points as suggested by these criteria were put in the boundary layers to account for NOB and rotational effects.

III. NON-OBERBECK–BOUSSINESQ EFFECTS IN THE NON-ROTATING CASE

This section is devoted to non-rotating Rayleigh–Bénard convection of water. Several authors have studied NOB effects by means of experiments[10,11] and two-dimensional numerical simulations.[13] Here, we present results from three-dimensional DNS, which also serve as reference for our investigation on the rotating case.

Probably the most prominent and best analyzed NOB effect is the increase of the temperature within the bulk, which can clearly be seen in Fig. 2 and in the mean temperature profiles in Fig. 3(a). The higher the applied temperature difference Δ, the hotter the fluid inside the Rayleigh–Bénard cell. This effect can be evaluated quantitatively by analyzing the center temperature, i.e., the radially,

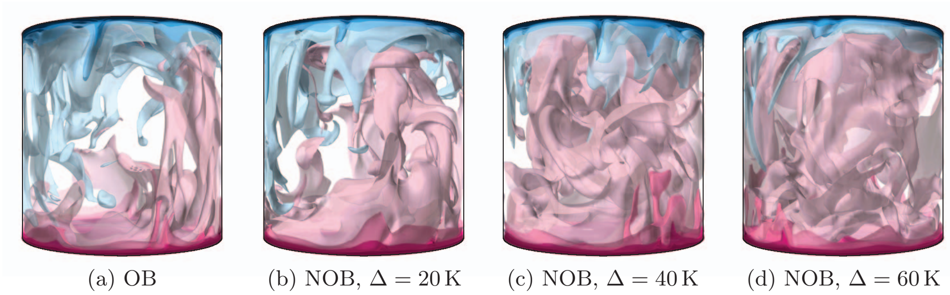

FIG. 2. Instantaneous temperature fields for $Ra = 10^8$ without rotation under (a) OB conditions and three different NOB conditions, (b) $\Delta = 20\,\mathrm{K}$, (c) $\Delta = 40\,\mathrm{K}$, and (d) $\Delta = 60\,\mathrm{K}$. Visualized are isosurfaces for ten equidistantly distributed values between the top and bottom temperature, T_t and T_b. Pink corresponds to temperatures above the mean temperature T_m and blue to temperatures below T_m.

azimuthally, and temporally averaged temperature at mid-height,

$$T_c \equiv \langle T \mid_{z=H/2} \rangle_{r,\phi,t}. \tag{10}$$

In Fig. 3(b), we present T_c obtained by our DNS for $Ra \in \{10^7, 10^8, 10^9\}$ for temperature differences Δ between 10 K and 70 K. T_c increases with Δ. For $\Delta = 70\,\mathrm{K}$ T_c is about 5.5 K higher than in the OB case. For comparison, the experimental data by Ahlers *et al.*[10] for $10^9 \lesssim Ra \lesssim 10^{11}$ and the two-dimensional DNS results by Sugiyama *et al.*[13] for $Ra = 10^8$ are also shown. All three data sets are in excellent agreement and, moreover, there is no significant dependence on the Rayleigh number for the cases considered.

Several models[10,31–33] have been proposed to predict T_c, however, the suitability of the model strongly depends on the fluid.[6,8] In the case of water, an extension of the Prandtl–Blasius boundary layer theory to non-constant viscosity ν and thermal diffusivity κ has been proven to be very successful.[10,13] The prediction of this theory is also depicted in Fig. 3(b). Since the variation of κ is rather small compared to the variation of ν with temperature, this also supports the hand-wavy explanation of the enhanced T_c: The fluid at the bottom is warmer, thus, in comparison to OB convection, the viscosity is lower and, thus, the fluid and the plumes emerging from the bottom boundary layer are more mobile, i.e., they are able to cross the cell faster. Furthermore, they also spend less time in contact with the ambient fluid and, hence, have less time to cool down. The analogue is true for the cold plumes from the top; their viscosity is higher, they move slower and they have more time to warm up in the bulk. As a consequence, the temperature in the center of the cell enhances. This suggests, that in the case of water the viscosity is the major reason for an increase of T_c with Δ.

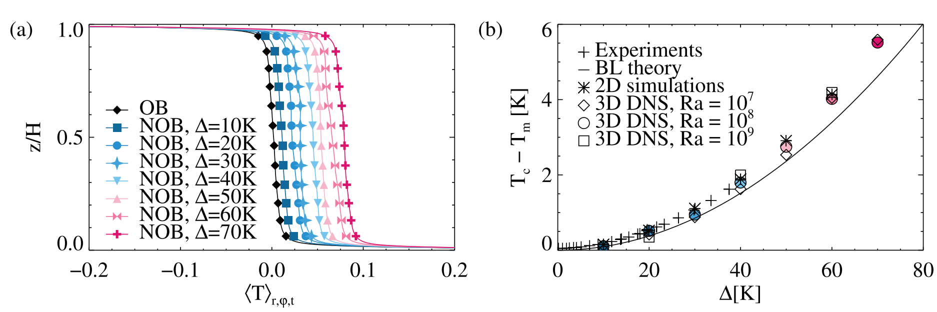

FIG. 3. (a) Mean temperature profiles for $Ra = 10^8$ under OB and various NOB conditions, $\Delta \in \{10\,\mathrm{K}, 20\,\mathrm{K}, 30\,\mathrm{K}, 40\,\mathrm{K}, 50\,\mathrm{K}, 60\,\mathrm{K}, 70\,\mathrm{K}\}$, without rotation. Note that not the full temperature range is shown. (b) Deviation of the center temperature T_c from the mean temperature T_m as function of the temperature difference Δ. The pluses show the experimental data by Ahlers *et al.*,[10] the asterisks represent the two-dimensional numerical data by Sugiyama *et al.*[13] for $Ra = 10^8$, the solid dashed line is the prediction by the extended Prandtl–Blasius boundary layer theory.[10] Our DNS data obtained for $Ra = 10^7$, 10^8, and 10^9 are denoted by diamonds, circles, and squares, respectively.

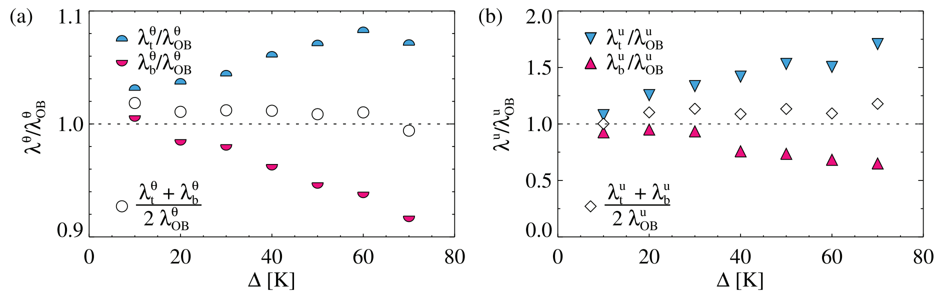

FIG. 4. Boundary layer thicknesses in the NOB case normalized by the boundary layer thickness in the OB case for $Ra = 10^8$. Their calculation is based on the slope criterion, cf. Eqs. (11)–(12). (a) Thermal boundary layer thicknesses, upper half circles: top thermal boundary layer λ_t^θ, lower half circles: bottom thermal boundary layer λ_b^θ, circles: ratio of the sum of the NOB to the OB boundary layer thicknesses. (b) Viscous boundary layer thicknesses, downward triangles: top viscous boundary layer λ_t^u, upward triangles: bottom viscous boundary layer λ_b^u, diamonds: ratio of the sum of the NOB to the OB boundary layer thicknesses.

Another very well-known feature of NOB convection is the different boundary layer thicknesses at the top and bottom. They are presented in Fig. 4. The boundary layer thicknesses are defined by the slope criterion,[34] i.e., they are determined by the point where the tangent of the profile at the plate intersects with either the center temperature, in the case of thermal boundary layers, or with the maxima of the radial velocity, in the case of viscous boundary layers. Mathematically expressed, the thermal top and bottom boundary layer thicknesses are given by

$$\lambda_t^\theta = \frac{T_t - T_c}{\partial_z \langle T \rangle_{r,\phi,t}\big|_{z=H}}, \qquad \lambda_b^\theta = \frac{T_c - T_b}{\partial_z \langle T \rangle_{r,\phi,t}\big|_{z=0}}, \tag{11}$$

and similarly the viscous ones are given by

$$\lambda_t^u = -\frac{u_r^{\max_t}}{\partial_z \langle u_r \rangle_{r,\phi,t}\big|_{z=H}}, \qquad \lambda_b^u = \frac{u_r^{\max_b}}{\partial_z \langle u_r \rangle_{r,\phi,t}\big|_{z=0}}, \tag{12}$$

where $u_r^{\max_t}$ and $u_r^{\max_b}$ are the first maxima of the radial velocity profile close to the top and bottom plate, respectively. In the OB case, the top and bottom boundary layers have, of course, the same thickness,

$$\lambda_{OB} = \lambda_t = \lambda_b. \tag{13}$$

In the NOB case, on the contrary, the top boundary layers are always thicker than the bottom ones. Furthermore, they exhibit the very peculiar behavior, that the sum of their thicknesses approximately equals the sum of the thicknesses in the OB case, i.e.,

$$\lambda_t + \lambda_b \approx 2\lambda_{OB}. \tag{14}$$

This holds for both, the viscous and the thermal boundary layer thicknesses. To be more precise, their ratio $(\lambda_t + \lambda_b)/(2\lambda_{OB})$ equals 1.009 ± 0.007 for the thermal and 1.10 ± 0.06 for the viscous boundary layer thicknesses. Thus, for both types the sum of OB boundary layer thicknesses is slightly greater than the sum of the NOB ones and approximation (14) works better for the thermal boundary layers. For some time it was suspected that Eq. (14) is a universal NOB behavior,[10] however, for example, in the case of glycerol this relation does not hold at all.[8,12]

Finally, the dimensionless heat flux, the Nusselt number, defined by

$$Nu = (RaPr\gamma)^{1/2} \langle u_z T \rangle - \gamma^{-1} \langle \Lambda \partial_z T \rangle \tag{15}$$

is shown in Fig. 5(a) as function of Ra for the OB case and the NOB case with $\Delta = 40\,\mathrm{K}$ and compared to experimental data by Funfschilling *et al.*[35] and the predictions by the Grossmann–Lohse (GL) theory.[4,36–39] The Nusselt number in our DNS is evaluated using the mean value of the r-ϕ plane averaged heat fluxes for all vertical z positions[40] and the error bars indicate the standard deviation. The Nusselt number according to the GL theory is calculated using the updated

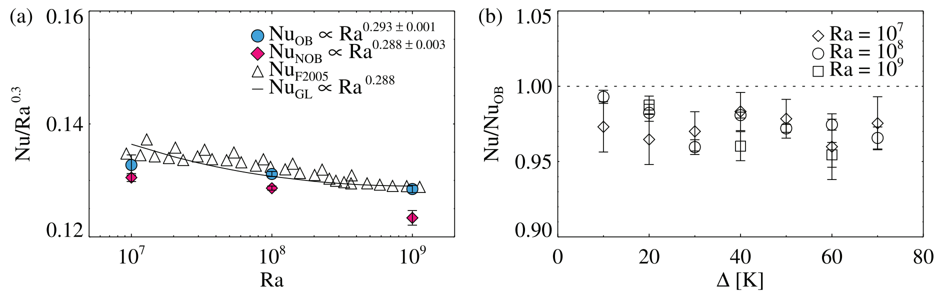

FIG. 5. (a) Reduced Nusselt number $Nu/Ra^{0.3}$ as function of Ra under OB (circles) and NOB conditions with $\Delta = 40\,$K. Additionally, the experimental data by Funfschilling *et al.*[35] and the predictions by the Grossmann–Lohse theory[36] are presented. (b) Nusselt number Nu_{NOB} for various NOB conditions normalized by the value under OB conditions Nu_{OB} as function of Δ; diamonds: $Ra = 10^7$, circles: $Ra = 10^8$, squares: $Ra = 10^9$. The Nusselt numbers were obtained by the mean value of the r-ϕ plane averaged heat fluxes for all vertical z positions. The error bars indicate the standard deviation.

prefactors by Stevens *et al.*[39] There is a good agreement of the experimental data, the OB DNS results and with the GL theory. The Nusselt number in the case of temperature-dependent material properties, Nu_{NOB}, is always slightly lower than in the pure OB case, Nu_{OB}. But despite that fact, the deviation and especially its scaling with Ra is only marginal, i.e., $Nu_{OB} \propto Ra^{0.293\,\pm\,0.001}$ compared to $Nu_{NOB} \propto Ra^{0.288\,\pm\,0.003}$. And even for higher Δ, as depicted in Fig. 5(b), the deviation remains below 5%. The insensitivity of the Nusselt number can be understood by expressing Nu in terms of the temperature gradient at the plates, which yields

$$Nu_{OB} = \frac{H}{2\lambda_{OB}}, \tag{16}$$

in the OB case, and similarly

$$Nu_{NOB} = \frac{H}{\lambda_t^\theta + \lambda_b^\theta} \frac{\Lambda_t \Delta_t + \Lambda_b \Delta_b}{\Lambda_m \Delta} \tag{17}$$

in the NOB case, with $\Delta_t = T_c - T_t$ and $\Delta_b = T_b - T_c$ being the top and bottom temperature drop, respectively. Hence, the following relation holds:[10]

$$\frac{Nu_{NOB}}{Nu_{OB}} = \frac{2\lambda_{OB}}{\lambda_t^\theta + \lambda_b^\theta} \frac{\Lambda_t \Delta_t + \Lambda_b \Delta_b}{\Lambda_m \Delta} = F_\lambda F_\Delta. \tag{18}$$

By inserting approximation (14), the first factor F_λ equals one. By using the exact values obtained from our DNS it is slightly less than one. Since there is also no strong temperature-dependence of Λ, the second factor F_Δ depends only weakly on Δ and is likewise close to one. However, one can even show, that F_Δ is also always less than one, since the center temperature is always higher than the mean temperature. Thus, even though, there is only a weak dependence of Nu on Δ, Nu_{NOB} is necessarily smaller than Nu_{OB}.

IV. NON-OBERBECK–BOUSSINESQ EFFECTS IN THE ROTATING CASE

In the following, we discuss how the flow changes when the Rayleigh–Bénard cell is rotated both with constant and with temperature-dependent material properties.

A. Flow structures and temperature distribution

When a constant rotation rate is applied, the typical plume shape changes. The plumes become more and more elongated with increasing $1/Ro$. For smaller $1/Ro$ a single large-scale circulation (LSC) is the predominant structure, for higher $1/Ro$ the LSC breaks down[41] and a regular pattern of columnar vortex structures forms. These columnar vortices are also called Ekman vortices[42–44] or convective Taylor columns.[45,46] This change of the flow behavior is visualized by

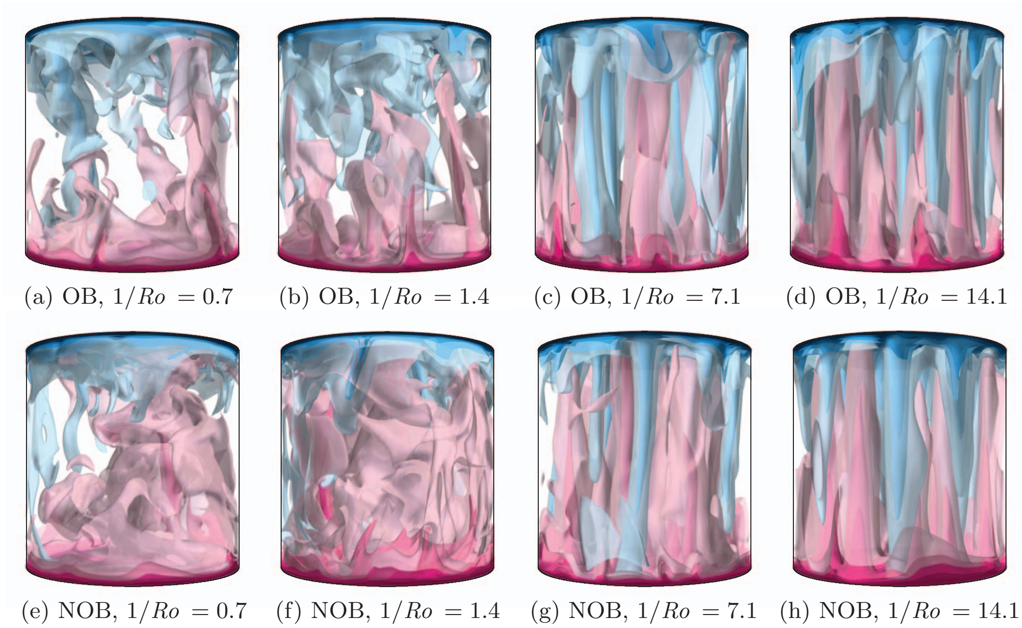

FIG. 6. Instantaneous temperature fields for $Ra = 10^8$. Visualized are isosurfaces for ten equidistantly distributed values between the top and bottom temperature, T_t and T_b. Pink corresponds to temperatures above the mean temperature T_m and blue to temperatures below T_m. The upper panel, (a)–(d), shows the OB cases, the lower panel, (e)–(h), shows the NOB cases with $\Delta = 40\,$K. The rotation rate increases from left to right. (a) and (e) $1/Ro = 0.7$; (b), (f) $1/Ro = 1.4$; (c) and (g) $1/Ro = 7.1$; and (d) and (h) $1/Ro = 14.1$. The corresponding non-rotating flow fields with $1/Ro = 0$ are presented in Figs. 2(a) and 2(c), respectively.

temperature isosurfaces in Fig. 6 for $Ra = 10^8$ and four representative inverse Rossby numbers, $1/Ro \in \{0.7, 1.4, 7.1, 14.1\}$ under OB and NOB conditions with $\Delta = 40\,$K.

In the NOB cases for low and moderate rotation rates, $1/Ro \lesssim 1.4$, the bulk of the fluid shows a generally higher temperature, similar as without rotation.[47] However, for even higher rotation rates, at the point when the columnar vortices become very pronounced, $1/Ro \gtrsim 7.1$, the differences in the temperature fields become less apparent. To investigate this in more detail, we analyze the mean temperature profiles, see Fig. 7, the mean temperature gradients, Fig. 8(a), and the center temperature T_c as function of $1/Ro$, Fig. 8(b).

Similar as in Sec. III, profiles, the temperature gradients, and T_c were obtained by averaging over full horizontal planes. This means, we include the sidewall boundary layers. Even though their contribution, in particular in rotating convection,[21,48] is certainly of importance, a detailed investigation of NOB effects inside them would go beyond the scope of this paper and we leave this for future work.

Both the profiles in Fig. 7 in the OB and in the NOB case show a non-zero mean temperature gradient within the bulk. This was found to be a result of vortex-vortex interactions.[49,50] More precisely, at fast enough rotation, when the columnar vortices appear, the flow is nearly two-dimensional and, thus, there is hardly any mixing in vertical direction. The only mixing occurs when vortices merge, which occurs along their lateral extent, i.e., in horizontal direction. Unlike without rotation, there is no fully three-dimensional mixing and consequently, there is a non-zero temperature gradient in the core part of the convection cell. The mean temperature gradient in the center of the cell, $\partial_z \langle T \rangle_{r,\phi,z}|_{z=H/2}$, is determined by making a linear fit on the mean temperature profiles in the range $0.4 \leq z/H \leq 0.6$ and presented in Fig. 8(a). In general, the absolute value of it increases with the rotation rate, and tends to be slightly higher in the NOB cases.

Under NOB conditions the profiles in Fig. 7 possess another intriguing feature. With increasing rotation rate, the temperature in the bulk decreases and the OB and NOB profiles for $1/Ro = 14.1$ approach each other.

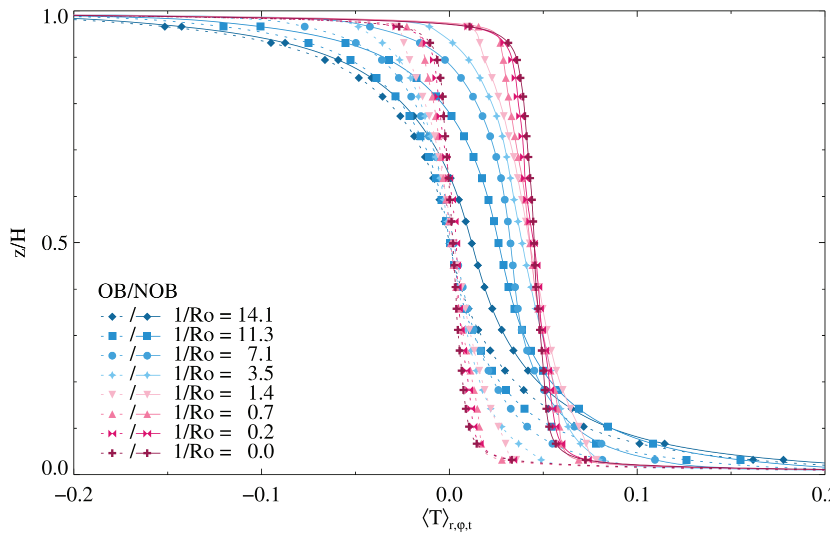

FIG. 7. Mean temperature profiles for $Ra = 10^8$. The dotted lines show the OB profiles, the solid lines the NOB ones with $\Delta = 40$ K. The color changes from blue to purple with decreasing rotation rate $1/Ro$. Note that not the full temperature range is shown.

Indeed, Fig. 8(b), displaying T_c as function of $1/Ro$, reveals that for high enough rotation rates, $1/Ro \gtrsim 3.5$, the center temperature shows a sudden drop (see also Table II). Physically, this is readily understood. Under strong rotation the relative magnitude of the viscous term in the Navier–Stokes equations (6) is small and thus, viscous effects in the bulk are less important.[18] But as explained in Sec. III, the increase of the T_c is almost solely due to the viscosity. We have performed a power-law fit based on the least squares method. It yielded that $T_c - T_m$ decreases approximately as $1/Ro^{0.66}$. However, it cannot decrease limitless, but probably reaches at most a value corresponding to the pure conductive state, which is still greater than T_m.

B. Boundary layers

For rotating convection, we can also define the boundary layer thicknesses based on the slope criterion similar to non-rotating convection. This is straightforward in the case of the viscous boundary layers by using Eq. (12). A selection of the radial velocity profiles used for the analysis is presented in Fig. 9(a). There is an anticipated asymmetry in the top and bottom NOB profiles. Figure 9(a) reveals further that the magnitude of the area-averaged radial velocity near the top and

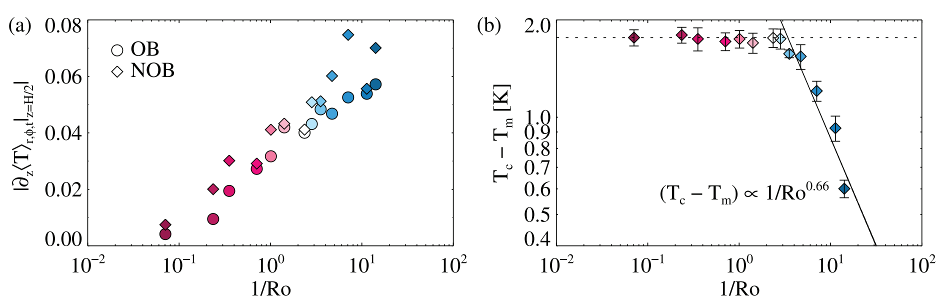

FIG. 8. (a) Absolute value of the mean temperature gradient $|\partial_z \langle T\rangle_{r,\phi,t}|_{z=H/2}|$ for $Ra = 10^8$, obtained by a linear fit of the mean temperature profiles between $0.4 \leq z/H \leq 0.6$. The circles denote the OB case, the diamonds the NOB case with $\Delta = 40$ K (b) Deviation of the center temperature T_c from the mean temperature T_m as function of the inverse Rossby number $1/Ro$ for $Ra = 10^8$ under NOB conditions with $\Delta = 40$ K. The dashed line represents the value in the non-rotating case, $1/Ro = 0$, the solid line shows a power law fit for $2.8 \leq 1/Ro \leq 14.1$.

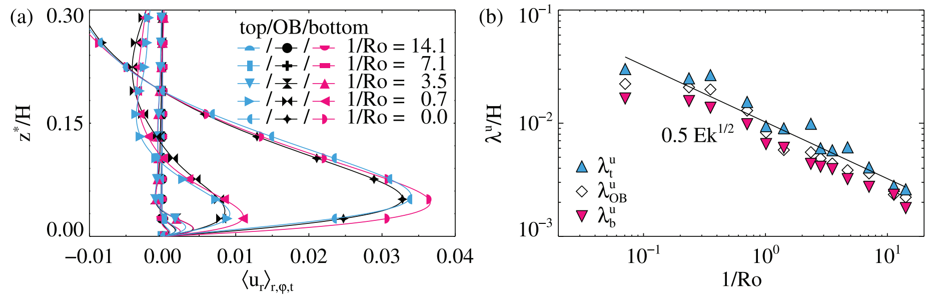

FIG. 9. (a) Mean profiles of the radial velocity, $\langle u_r\rangle_{r,\phi,t}$, for $Ra = 10^8$ under OB and NOB conditions with $\Delta = 40$ K and various $1/Ro$. The ordinate shows the distance z^* from the top and bottom plate, respectively, i.e., the profiles under NOB conditions of the upper half of the cell are mirrored along the midplane. The OB profiles were obtained by averaging the upper and lower profiles. Open symbols with solid lines: NOB profiles for the upper half of the cylinder. (b) Viscous boundary layer thicknesses based on the slope criterion (12) as function of the inverse Rossby number $1/Ro$; diamonds: OB boundary layer thicknesses λ^u_{OB}, upward triangles: top NOB boundary layer thicknesses λ^u_t, downward triangles: bottom NOB boundary layer thicknesses λ^u_b. The solid line shows the Ekman scaling $0.5Ek^{1/2}$.

bottom plates decreases with increasing rotation rate, which indicates a breakdown of the large-scale circulation that is essential for non-rotational thermal convection in water for $Ra = 10^8$.

The maxima for increasing $1/Ro$ are closer to the top and bottom wall, respectively, a behavior also reflected in the viscous boundary layer thicknesses λ^u presented in Fig. 9(b). The viscous boundary layer thickness λ^u decreases with higher rotation rates and it is well-known, that in rapidly rotating flows the viscous boundary layer is an Ekman type boundary layer with a thickness proportional to $Ek^{1/2}$. In fact, λ^u_{OB} follows $0.5Ek^{1/2}$ perfectly well for $1/Ro \gtrsim 0.7$. Under NOB conditions, the drop of λ^u_t occurs at higher $1/Ro$ than in the OB case and $\lambda^u_t > \lambda^u_{OB}$ for all Ro. On the contrary, the drop of λ^u_b occurs for lower $1/Ro$ than in the OB case and $\lambda^u_b < \lambda^u_{OB}$ for all $1/Ro$. The deviation is only small and the scaling exponent of Ek is essentially the same in the OB and the NOB cases. Moreover, the sum of the top and bottom boundary layer thicknesses in the NOB cases still approximately equals their sum in the OB cases. But it is not too surprising that in opposite to the center temperature T_c, the thicknesses of the viscous boundary layers keep on being non-negligibly influenced by the temperature-dependence of the viscosity. In the Ekman layer, the Coriolis force is balanced by the pressure gradient and the viscous shear.[18] Friction acts to satisfy the no-slip condition at the plates, hence, in the boundary layers the viscous processes are essential, despite the fact that Coriolis force dominates the bulk.[19]

The definition of the thermal boundary layer thickness is more tricky.[51] Instead of using Eq. (11), Stevens, Clercx, and Lohse[51] suggested to use the intersection of the tangent to the mean temperature profile at the plate and of the tangent to the profile at the center of the cell,

$$\tilde{\lambda}^\theta_t = \frac{T_t - T_c - \partial_z\langle T\rangle_{r,\phi,t}\big|_{z=H/2} H/2}{\partial_z\langle T\rangle_{r,\phi,t}\big|_{z=H} - \partial_z\langle T\rangle_{r,\phi,t}\big|_{z=H/2}}, \quad \tilde{\lambda}^\theta_b = \frac{T_c - T_b - \partial_z\langle T\rangle_{r,\phi,t}\big|_{z=H/2} H/2}{\partial_z\langle T\rangle_{r,\phi,t}\big|_{z=0} - \partial_z\langle T\rangle_{r,\phi,t}\big|_{z=H/2}}. \tag{19}$$

The boundary layer thicknesses based on both definitions are presented in Fig. 10. Definition (11) has the advantage that it allows for some analytical discussion of the Nusselt number, presented in Sec. IV C. Definition (19) on the other hand is more physical since it takes the mean temperature gradient into account. But the essential behavior is very similar: λ^θ and $\tilde{\lambda}^\theta$ are almost constant for $1/Ro \lesssim 0.35$, decrease for $0.35 \lesssim 1/Ro \lesssim 7.1$, and then sharply increase for $1/Ro \gtrsim 7.1$. Remarkably, for $1/Ro > 7.1$ the bottom NOB boundary layers are thicker than the top ones and than the OB boundary layers, whereas the top boundary layers are thinner than the OB boundary layers and consequently, also as the bottom NOB boundary layers. Hence, for fast rotation the situation is reversed to slow and moderate rotation. In addition we also plotted the line $0.5Ek^{1/2}$ and the point of intersection between λ^u and λ^θ and between λ^u and $\tilde{\lambda}^\theta$ is determined to be at $1/Ro \approx 1.4$. But this inverse Rossby number does not seem to be crucial for any observed change in a flow feature.

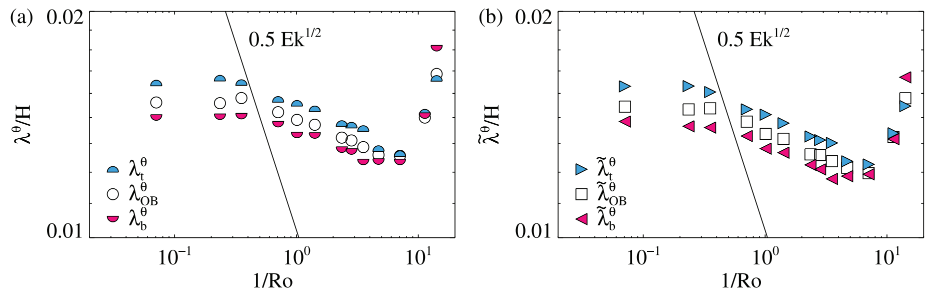

FIG. 10. (a) Thermal boundary layer thicknesses based on the slope criterion (11) as function of the inverse Rossby number $1/Ro$; circles: OB boundary layer thicknesses λ^θ_{OB}, upper half circles: top NOB boundary layer thicknesses λ^θ_t, lower half circles: bottom NOB boundary layer thicknesses λ^θ_b. (b) Thermal boundary layer thicknesses based on the slope criterion that considers the mean temperature gradient in the bulk (19) as function of the inverse Rossby number $1/Ro$; squares: OB boundary layer thicknesses $\tilde{\lambda}^\theta_{OB}$, right facing triangles: top NOB boundary layer thicknesses $\tilde{\lambda}^\theta_t$, left facing triangles: bottom NOB boundary layer thicknesses $\tilde{\lambda}^\theta_b$. The solid line in both panels shows the Ekman scaling $0.5Ek^{1/2}$, similar as in Fig. 9(b).

Additionally, we also evaluated the boundary layer thicknesses based on the rms profiles for the temperature and the radial velocity,[52,53] shown in Fig. 11. The thicknesses are then defined by

$$\delta^\theta_t = H - \max\left(z|_{\partial_z\langle u_{r,rms}\rangle=0}\right), \qquad \delta^\theta_b = \min\left(z|_{\partial_z\langle u_{r,rms}\rangle=0}\right), \tag{20}$$

$$\delta^u_t = H - \max\left(z|_{\partial_z\langle T_{rms}\rangle=0}\right), \qquad \delta^u_b = \min\left(z|_{\partial_z\langle T_{rms}\rangle=0}\right), \tag{21}$$

and presented in Fig. 12. When the viscous boundary layer thickness is based on the rms criterion, the scaling is still consistent with the Ekman scaling, i.e., $\delta^u \propto Ek^{1/2}$, however, the absolute value and thus the prefactor is higher. This was also found by Stevens *et al.*[42] and Kunnen, Geurts, and Clercx.[53] According to King, Stellmach, and Aurnou,[19] the thermal and viscous Ekman boundary layers should have the same thickness, $\delta^\theta = \delta^u$, somewhere between $6 \lesssim Pr^{3/4}Ra^{1/4}Ro^{3/2} \lesssim 20$, or expressed explicitly in terms of $1/Ro$ and for $Pr = 4.38$ and $Ra = 10^8$, it should be between $6.25 \lesssim 1/Ro \lesssim 14.3$. We mark this predicted crossover range by a gray shaded area. Indeed, our OB DNS results agree nicely with this prediction. We estimate the crossover Rossby number to be $1/Ro \approx 7.9$. Under NOB conditions, the crossover of the top boundary layers occurs for higher $1/Ro$ than the OB crossover, whereas, the crossover of the bottom boundary layers occurs for smaller $1/Ro$ than the OB crossover. In addition, similar as for the λ^θ and $\tilde{\lambda}^\theta$, the top boundary layers are thicker than the bottom ones for $1/Ro > 7.1$. Furthermore, the inverse Rossby number $1/Ro$ where λ^θ and $\tilde{\lambda}^\theta$ show the sudden increase and their respective thicknesses reverses coincides with the inverse Rossby number where $\delta^\theta = \delta^u$, i.e., $1/Ro \approx 7.9$.

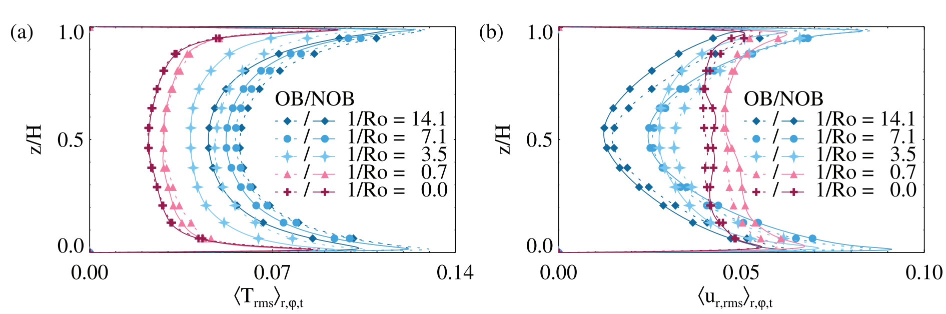

FIG. 11. (a) Mean profiles of the rms temperature for various inverse Rossby numbers $1/Ro$, including no rotation, $1/Ro = 0$. The dotted lines show the OB cases, the solid lines the NOB cases. (b) Mean profiles of the radial rms velocity. Analogous to Fig. (a), the dotted lines show the OB cases, the solid lines the NOB cases.

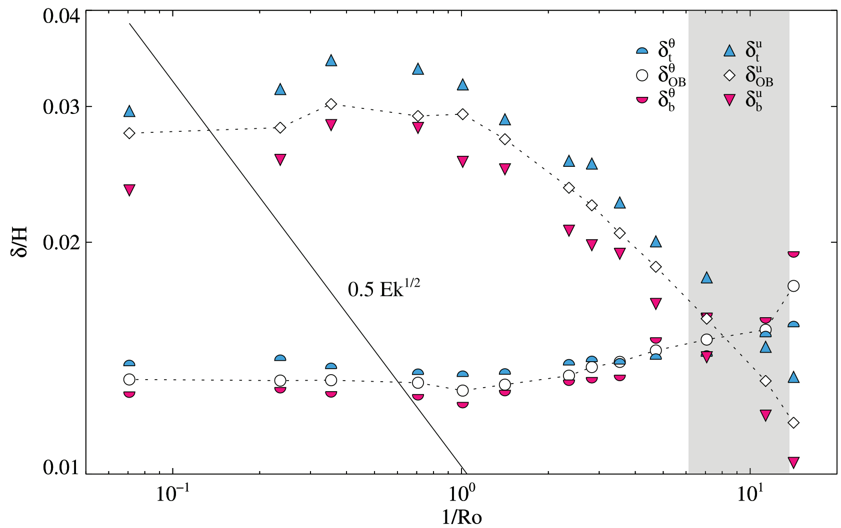

FIG. 12. Thermal and viscous boundary layer thicknesses based on the maxima of the rms temperature and velocity profiles, (20) and (21), respectively, as function of the inverse Rossby number $1/Ro$. Circles: OB thermal boundary layer thicknesses δ^θ_{OB}, upper half circles: top NOB thermal boundary layer thicknesses δ^θ_t, lower half circles: bottom thermal NOB boundary layer thicknesses δ^θ_b. Diamonds: OB viscous boundary layer thicknesses δ^u_{OB}, upward triangles: top NOB viscous boundary layer thicknesses δ^u_t, downward triangles: bottom NOB viscous boundary layer thicknesses δ^u_b. The solid line shows the Ekman scaling $0.5Ek^{1/2}$, similar as in Fig. 9(b). The dashed lines are guides to the eye. The gray shaded area shows the crossover range of the boundary layer thicknesses predicted by King, Stellmach, and Aurnou.[19]

C. Heat flux

Finally, we discuss how the Nusselt number is influenced by temperature-dependent material properties in rotating Rayleigh–Bénard convection. The Nusselt number Nu normalized by its value without rotation Nu^0 as function of the inverse Rossby number $1/Ro$ is shown in Fig. 13.

Under OB conditions the dependence of the heat flux on the rotation rate has been subject to a plethora of experimental and numerical studies.[20,44,54–60] It is generally approved that there are essentially two competing mechanisms that determine how Nu changes with $1/Ro$ for fluids with $Pr \gtrsim 1$. On the one hand there is Ekman pumping, leading to an enhancement of the heat transport and on the other hand there is the Taylor–Proudman effect,[61,62] resulting in the suppression of the heat transport. Hence, one often distinguishes between three different regimes,[7,21,44] indicated by the roman numbers I, II, and III in Fig. 13.

For low rotation rates, denoted as regime I, the Nusselt numbers in the rotating and in the non-rotating case are virtually the same. Hence, the system is governed by the buoyancy force. For more rapid rotation, regime II, there is a sudden increase of Nu and then, after reaching a maximum which marks the transition to regime III, the heat transport drops rapidly. The transition from regimes I to II was found to be a bifurcation and a finite size effect of the Rayleigh–Bénard cell.[43,58] The critical inverse Rossby number for this transition was determined to

$$\frac{1}{Ro_c} = \frac{a}{\Gamma}\left(1 + \frac{b}{\Gamma}\right), \qquad a = 0.381,\ b = 0.061 \tag{22}$$

which results in $1/Ro_c = 0.4$ for our case of $\Gamma = 1$.

The enhancement of the heat transport in regime II is commonly understood to be due to the formation of columnar vortex structures. They suck additional heat out of the thermal boundary layer,[23,49,50,53,56] a process called Ekman pumping. The decrease in regime III is explained with help of the Taylor–Proudman theorem. It states that for very rapid rotation all steady slow motions in an inviscid fluid are two-dimensional, in other words, that all components of the velocity are not allowed to vary in the direction of the rotation axis.[63] Strictly speaking the Taylor–Proudman theorem is not valid in the time-dependent convective flow considered here. Nonetheless, the tendencies are correctly captured by it. In this regime, the system is expected to behave as if it was in geostrophic

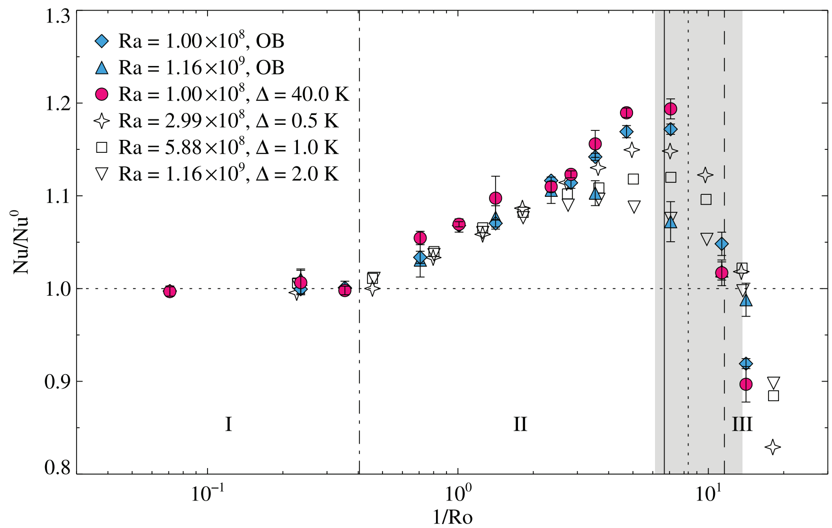

FIG. 13. Nusselt number Nu in the rotating case normalized with the Nusselt number in the non-rotating case Nu^0 as function of the inverse Rossby number $1/Ro$. The filled diamonds show the OB DNS data for $Ra = 10^8$, the filled circles the NOB data for $\Delta = 40$ K and the same Ra, and the filled upward triangles OB data for $Ra = 1.16 \times 10^9$. For comparison the open stars, squares, and downward triangles show experimental data by Kunnen *et al.*[21] for $Ra = 2.99 \times 10^8$, 5.88×10^8, and 1.16×10^9, respectively, for the same $Pr = 4.38$. The vertical dotted dashed line shows the onset of heat transfer enhancement predicted by Weiss *et al.*[43] The other three vertical lines show predictions for the transition to the rotation dominated regime, triple-dotted dashed line: Kunnen *et al.*,[21] dashed line: Ecke and Niemela,[54] dotted line: Julien *et al.*[20] The gray shaded area represents the crossover range of the boundary layer thicknesses according to King, Stellmach, and Aurnou,[19] as in Fig. 12.

balance. However, the exact border between the regimes II and III is slightly arbitrary and several combinations of the control parameters have been proposed to determine whether the flow is rotation or buoyancy dominated.[19,20,23,52,54,57,64] Furthermore, the heat flux is not the only way to characterize this transition but there are also other approaches, e.g., using the helicity,[64] the strength of the large-scale circulation,[42] or the toroidal and poloidal energy.[29]

In Fig. 13, we compare our DNS results for $Ra = 10^8$ and $Ra = 1.19 \times 10^9$ to experimental data and several recent predictions for the regime transitions. As previously, the Nusselt number was obtained by the mean value of the r-ϕ plane averaged Nu for all vertical z positions.

The agreement with the experimental data by Kunnen *et al.*[21] for $Ra = 1.19 \times 10^9$ and $Pr = 4.38$ is excellent. Furthermore, these authors have shown that their measurements also agree with the data by Zhong and Ahlers.[44] Unfortunately, neither group measured for Rayleigh numbers as low as ours or for temperature differences as high as our DNS under NOB conditions. However, the trend of the Nusselt number to an enhanced heat flux increase and a shift of this maximum to higher $1/Ro$ with decreasing Ra is captured nicely. The higher maximum for lower Ra is explained by a lower turbulent viscosity.[7]

The maximum heat flux for $Ra = 10^8$ is observed for $1/Ro \approx 7.1$, which is the same point, where the viscous Ekman and the thermal boundary layers intersect, $\delta^u = \delta^\theta$. This impact of the boundary layer dynamics in rotating Rayleigh–Bénard convection on the global heat transport was first suggested by Rossby[23] and later on taken up by others, e.g., King, Stellmach, and Aurnou,[19] Julien *et al.*,[49] and King *et al.*[52] According to King, Stellmach, and Aurnou,[19] the crossover of the boundary layers is supposed to mark the transition of the heat transport behaving either quasigeostrophic or weakly rotating. Similar as in Fig. 12, the proposed transition range for $Ra = 10^8$ is visualized by a gray-shaded area and fits nicely to our DNS. However, transitions in the scaling behavior of Nu with the rotation rate were also observed in numerical simulations with stress-free boundary conditions by Schmitz and Tilgner[57] where no Ekman boundary layers are present. It might be worthwhile testing whether a generalization in terms of dissipation layers suggested by Petschel *et al.*[65] for non-rotating Rayleigh–Bénard convection can be found.

Other authors proposed transition parameters that were supposed to be independent of the boundary conditions. Julien *et al.*[20] suggested an approach based on an asymptotic state in the limit $Ek \to 0$ which is expected to be valid for Ekman numbers still about one magnitude lower than ours for $Ra = 10^8$. Nonetheless their prediction of the transitional regime with active Ekman pumping, given by $1 \gtrsim Ro \gtrsim Pr^{1/8}Ra^{-1/8}$, yielding $1 \lesssim 1/Ro \lesssim 8.3$ for $Ra = 10^8$, matches the maximum Nu decently. Ecke and Niemela[54] empirically determined the transition to geostrophic turbulence by measurements in helium with $Pr = 0.7$. There, the thermal boundary layer is always thicker than the viscous one, thus, the argumentation of a crossover of boundary layers does, of course, not apply. But despite that, their transitional Rossby number $1/Ro_t = 1.5Pr^{1/2}Ra^{1/14}$, which gives 11.7 for $Ra = 10^8$, also coincides in a good approximation with the Rossby number where the thermal boundary layers based on the slope criterion start to increase, where the rms boundary layer thicknesses intersect and the maximum of the Nusselt number is found.

Now the question arises in which way NOB effects influence the heat transport in rotating convection. Fig. 13 shows that Nu_{NOB} normalized by its value without rotation Nu^0_{NOB} is virtually the same and agrees within the statistical error with Nu_{OB}/Nu^0_{OB} for $1/Ro \lesssim 3.5$. Thus, the temperature dependence of the material properties influences the Nusselt number in the same way as without rotation. However, in the small range between $3.5 \lesssim 1/Ro \lesssim 11.3$, the ratio Nu_{NOB}/Nu^0_{NOB} is greater than Nu_{OB}/Nu^0_{OB}. This does not mean that the actual Nusselt number is larger, Nu_{NOB} is only at most as large as Nu_{OB} within the statistical error as can be seen in Table II. For $1/Ro \gtrsim 11.3$, the situation is reversed, i.e., $Nu_{NOB}/Nu^0_{NOB} < Nu_{OB}/Nu^0_{OB}$.

To understand this behavior, it is useful to consider again Eq. (18), i.e., the separation of the ratio Nu_{NOB}/Nu_{OB} into a contribution by the boundary layers, F_λ, and a contribution by the temperature drops, F_Δ. The factor F_Δ is independent of $1/Ro$ for $1/Ro \lesssim 3.5$. For more rapid rotation, the center temperature T_c drops, as discussed before and was shown in Fig. 8(b), thus the top temperature drop Δ_t increases and the bottom temperature drop Δ_b decreases. Consequently, F_Δ decreases, but only marginally. The factor F_λ is also independent of $1/Ro$ for $1/Ro \lesssim 3.5$. Afterwards it increases, which is also the point where the thermal boundary layers in the NOB case intersect, as was presented in Fig. 10(a). F_λ has its maximum value of 1.03 for $1/Ro = 7.1$. For the highest $1/Ro$, when the top boundary layer thickness λ^θ_t is thinner than the bottom boundary layer thickness λ^θ_b, F_λ is smaller than in the non-rotating case. Hence, the influence on the boundary layers is crucial for Nu. The drop of T_c is only of minor importance.

V. SUMMARY AND CONCLUDING REMARKS

The influence of rotation on Rayleigh–Bénard convection in water was investigated by means of three-dimensional DNS. The temperature dependence of the density within the buoyancy force, the viscosity, and the heat conductivity and were considered explicitly and compared to the standard OB approximation. Hence, we were able to predict the importance of NOB effects. NOB effects manifest itself in a variety of ways, here we focused on the most prominent features, namely, the increase of the center temperature T_c, different boundary layer thicknesses and the modification of the dimensionless heat flux, the Nusselt number Nu.

Without rotation, T_c increases together with the applied temperature difference. It is well predicted by an extension of the Prandtl–Blasius boundary layer theory proposed by Ahlers *et al.*[10] This suggests that the temperature dependence of the viscosity is mainly responsible for the enhanced T_c. The top viscous and thermal boundary layers are always thicker than the bottom boundary layers, which is expected to be generally true for liquids. However, in gases this can be reversed.[66] In the special case of water at a temperature of $T_m = 40\,^\circ$C, the sum of the boundary layer thicknesses equals approximately the sum of the boundary layer thicknesses under perfect OB conditions. Furthermore, the Nusselt number Nu is lower under NOB conditions, but this deviation remains below 5%, even for temperature differences up to 70 K.

For low and moderate rotation rates, the Rayleigh–Bénard system responds very similar to the temperature dependencies of the material properties as without rotation. That is, T_c has the same value, the top thermal, and viscous boundary layers are thicker than the corresponding bottom ones and Nu_{NOB}/Nu_{OB} is the same as in the non-rotational case.

However, for rapid rotation, certain NOB effects, i.e., those caused by the viscosity are suppressed. The reason is that viscous effects in the bulk of the Rayleigh–Bénard cell become negligible for strong rotations rates. This is best reflected by the behavior of T_c that shows a sharp decrease for $1/Ro \gtrsim 3.5$. Although this might suggest that in experiments many symmetries being inherent in Rayleigh–Bénard convection are restored under NOB conditions if only the rotation rate is high enough, one has to be careful since it will probably be a fallacy. There, not only the centrifugal buoyancy, that was not considered in this study, would be another source of breaking of the top-bottom symmetry, including a higher center temperature,[25] but furthermore, the boundary layers keep on being strongly influenced by viscous forces. Under NOB conditions, the crossover of the top (bottom) thermal and viscous boundary layers happens for slightly larger (smaller) $1/Ro$ than under OB conditions. At this crossover Rossby number the absolute deviation between Nu_{OB} and Nu_{NOB} is minimal and smaller than without rotation. Moreover, at this $1/Ro$, the top thermal boundary layers become thinner than the bottom ones, whereas for the viscous boundary layer the situation remains as without rotation and the top viscous boundary layers are thicker than the bottom ones.

ACKNOWLEDGMENTS

The authors are very grateful to Professor E. Bodenschatz for his support and hospitality at the Max-Planck-Institute for Dynamics and Self-Organization in Göttingen. Furthermore, the authors acknowledge financial support by the Deutsche Forschungsgemeinschaft (DFG) under Grant No. SH405/2, in the framework of SFB 963/1, Project No. A6, and Heisenberg fellowship SH405/4. The authors would also like to thank the Leibniz-Rechenzentrum (LRZ) in Garching for providing computational resources.

[1] H. Bénard, "Les tourbillons cellulaires dans une nappe liquide," Rev. Gen. Sci. Pures Appl. **11**, 1261–1271 (1900).
[2] Lord Rayleigh, "On convection currents in a horizontal layer of fluid, when the higher temperature is on the under side," Phil. Mag. **32**, 529–546 (1916).
[3] E. Bodenschatz, W. Pesch, and G. Ahlers, "Recent developments in Rayleigh-Bénard convection," Annu. Rev. Fluid Mech. **32**, 709–778 (2000).
[4] G. Ahlers, S. Grossmann, and D. Lohse, "Heat transfer and large scale dynamics in turbulent Rayleigh-Bénard convection," Rev. Mod. Phys. **81**, 503 (2009).
[5] D. Lohse and K.-Q. Xia, "Small-scale properties of turbulent Rayleigh-Bénard convection," Ann. Rev. Fluid Mech. **42**, 335–364 (2010).
[6] F. Chillà and J. Schumacher, "New perspectives in turbulent Rayleigh-Bénard convection," Eur. Phys. J. E **35**, 1–25 (2012).
[7] R. J. A. M. Stevens, H. J. H. Clercx, and D. Lohse, "Heat transport and flow structure in rotating Rayleigh–Bénard convection," Eur. J. Mech. (B/Fluids) **40**, 41–49 (2013).
[8] S. Horn, O. Shishkina, and C. Wagner, "On non-Oberbeck–Boussinesq effects in three-dimensional Rayleigh–Bénard convection in glycerol," J. Fluid Mech. **724**, 175–202 (2013).
[9] S. Horn, O. Shishkina, and C. Wagner, "Non-Oberbeck–Boussinesq effects in Rayleigh–Bénard convection of liquids," *Third International Conference on Turbulence and Interactions* (Springer, 2013).
[10] G. Ahlers, E. Brown, F. Fontenele Araujo, D. Funfschilling, S. Grossmann, and D. Lohse, "Non-Oberbeck–Boussinesq effects in strongly turbulent Rayleigh–Bénard convection," J. Fluid Mech. **569**, 409–445 (2006).
[11] E. Brown and G. Ahlers, "Temperature gradients, and search for non-Boussinesq effects, in the interior of turbulent Rayleigh–Bénard convection," Europhys. Lett. **80**, 14001 (2007).
[12] K. Sugiyama, E. Calzavarini, S. Grossmann, and D. Lohse, "Non-Oberbeck–Boussinesq effects in two-dimensional Rayleigh-Bénard convection in glycerol," Europhys. Lett. **80**, 34002 (2007).
[13] K. Sugiyama, E. Calzavarini, S. Grossmann, and D. Lohse, "Flow organization in two-dimensional non-Oberbeck–Boussinesq Rayleigh-Bénard convection in water," J. Fluid Mech. **637**, 105–135 (2009).
[14] Y.-N. Young, H. Riecke, and W. Pesch, "Whirling hexagons and defect chaos in hexagonal non-Boussinesq convection," New J. Phys. **5**, 135 (2003).
[15] A. Oberbeck, "Ueber die Wärmeleitung der Flüssigkeiten bei Berücksichtigung der Strömungen infolge von Temperaturdifferenzen," Ann. Phys. **243**, 271–292 (1879).
[16] J. Boussinesq, *Théorie Analytique de la Chaleur* (Gauthier-Villars, Paris, 1903).
[17] D. D. Gray and A. Giorgini, "The validity of the Boussinesq approximation for liquids and gases," Int. J. Heat Mass Transfer **19**, 545–551 (1976).
[18] H. P. Greenspan, *The Theory of Rotating Fluids* (Cambridge University Press, London, 1968).
[19] E. M. King, S. Stellmach, and J. M. Aurnou, "Heat transfer by rapidly rotating Rayleigh–Bénard convection," J. Fluid Mech. **691**, 568–582 (2012).
[20] K. Julien, E. Knobloch, A. M. Rubio, and G. M. Vasil, "Heat transport in low-Rossby-number Rayleigh-Bénard convection," Phys. Rev. Lett. **109**, 254503 (2012).

[21] R. P. J. Kunnen, R. J. A. M. Stevens, J. Overkamp, C. Sun, G. F. van Heijst, and H. J. H. Clercx, "The role of Stewartson and Ekman layers in turbulent rotating Rayleigh–Bénard convection," J. Fluid Mech. **688**, 422–442 (2011).
[22] J.-Q. Zhong, R. J. A. M. Stevens, H. J. H. Clercx, R. Verzicco, D. Lohse, and G. Ahlers, "Prandtl-, Rayleigh-, and Rossby-Number dependence of heat transport in turbulent rotating Rayleigh–Bénard Convection," Phys. Rev. Lett. **102**, 044502 (2009).
[23] H. T. Rossby, "A study of Bénard convection with and without rotation," J. Fluid Mech. **36**, 309–335 (1969).
[24] G. Homsy and J. Hudson, "Centrifugally driven thermal convection in a rotating cylinder," J. Fluid Mech. **35**, 33–52 (1969).
[25] J. Hart and D. Ohlsen, "On the thermal offset in turbulent rotating convection," Phys. Fluids **11**, 2101 (1999).
[26] F. Marques, I. Mercader, O. Batiste, and J. Lopez, "Centrifugal effects in rotating convection: Axisymmetric states and three-dimensional instabilities," J. Fluid Mech. **580**, 303 (2007).
[27] J. Lopez and F. Marques, "Centrifugal effects in rotating convection: Nonlinear dynamics," J. Fluid Mech. **628**, 269–297 (2009).
[28] O. Shishkina and C. Wagner, "A fourth order accurate finite volume scheme for numerical simulations of turbulent Rayleigh–Bénard convection in cylindrical containers," C. R. Mecanique **333**, 17–28 (2005).
[29] S. Horn and O. Shishkina, "Toroidal and poloidal energy in rotating Rayleigh–Bénard convection," preprint arXiv:1404.7755 (2014).
[30] O. Shishkina, R. J. A. M. Stevens, S. Grossmann, and D. Lohse, "Boundary layer structure in turbulent thermal convection and its consequences for the required numerical resolution," New J. Phys. **12**, 075022 (2010).
[31] X. Z. Wu and A. Libchaber, "Non-Boussinesq effects in free thermal convection," Phys. Rev. A **43**, 2833–2839 (1991).
[32] J. Zhang, S. Childress, and A. Libchaber, "Non-Boussinesq effect: Thermal convection with broken symmetry," Phys. Fluids **9**, 1034–1042 (1997).
[33] M. Manga and D. Weeraratne, "Experimental study of non-Boussinesq Rayleigh–Bénard convection at high Rayleigh and Prandtl numbers," Phys. Fluids **11**, 2969–2976 (1999).
[34] S. Wagner, O. Shishkina, and C. Wagner, "Boundary layers and wind in cylindrical Rayleigh–Bénard cells," J. Fluid Mech. **697**, 336–366 (2012).
[35] D. Funfschilling, E. Brown, A. Nikolaenko, and G. Ahlers, "Heat transport by turbulent Rayleigh-Bénard convection in cylindrical samples with aspect ratio one and larger," J. Fluid Mech. **536**, 145–154 (2005).
[36] S. Grossmann and D. Lohse, "Scaling in thermal convection: A unifying theory," J. Fluid Mech. **407**, 27–56 (2000).
[37] S. Grossmann and D. Lohse, "Thermal convection for large Prandtl numbers," Phys. Rev. Lett. **86**, 3316–3319 (2001).
[38] S. Grossmann and D. Lohse, "Prandtl and Rayleigh number dependence of the Reynolds number in turbulent thermal convection," Phys. Rev. E **66**, 016305 (2002).
[39] R. J. Stevens, E. van der Poel, S. Grossmann, and D. Lohse, "The unifying theory of scaling in thermal convection: The updated prefactors," J. Fluid Mech. **730**, 295–308 (2013).
[40] O. Shishkina and C. Wagner, "Local heat fluxes in turbulent Rayleigh–Bénard," Phys. Fluids **19**, 085107 (2007).
[41] R. P. J. Kunnen, H. J. H. Clercx, and B. J. Geurts, "Breakdown of large-scale circulation in turbulent rotating convection," Europhys. Lett. **84**, 24001 (2008).
[42] R. J. A. M. Stevens, J.-Q. Zhong, H. J. H. Clercx, G. Ahlers, and D. Lohse, "Transitions between turbulent states in rotating Rayleigh–Bénard convection," Phys. Rev. Lett. **103**, 024503 (2009).
[43] S. Weiss, R. J. A. M. Stevens, J.-Q. Zhong, H. J. H. Clercx, D. Lohse, and G. Ahlers, "Finite-size effects lead to supercritical bifurcations in turbulent rotating Rayleigh–Bénard convection," Phys. Rev. Lett. **105**, 224501 (2010).
[44] J.-Q. Zhong and G. Ahlers, "Heat transport and the large-scale circulation in rotating turbulent Rayleigh–Bénard convection," J. Fluid Mech. **665**, 300–333 (2010).
[45] I. Grooms, K. Julien, J. B. Weiss, and E. Knobloch, "Model of convective Taylor columns in rotating Rayleigh-Bénard convection," Phys. Rev. Lett. **104**, 224501 (2010).
[46] E. M. King and J. M. Aurnou, "Thermal evidence for Taylor columns in turbulent rotating Rayleigh-Bénard convection," Phys. Rev. E **85**, 016313 (2012).
[47] S. Horn, O. Shishkina, and C. Wagner, "The influence of non-Oberbeck–Boussinesq effects on rotating turbulent Rayleigh–Bénard convection," J. Phys.: Conf. Ser. **318**, 082005 (2011).
[48] R. Kunnen, H. Clercx, and G. van Heijst, "The structure of sidewall boundary layers in confined rotating Rayleigh–Bénard convection," J. Fluid Mech. **727**, 509–532 (2013).
[49] K. Julien, S. Legg, J. McWilliams, and J. Werne, "Rapidly rotating turbulent Rayleigh–Bénard convection," J. Fluid Mech. **322**, 243–273 (1996).
[50] Y. Liu and R. Ecke, "Heat transport scaling in turbulent Rayleigh–Bénard convection: Effects of Rotation and Prandtl number," Phys. Rev. Lett. **79**, 2257–2260 (1997).
[51] R. J. A. M. Stevens, H. J. H. Clercx, and D. Lohse, "Boundary layers in rotating weakly turbulent Rayleigh–Bénard convection," Phys. Fluids **22**, 085103 (2010).
[52] E. M. King, S. Stellmach, J. Noir, U. Hansen, and J. M. Aurnou, "Boundary layer control of rotating convection systems," Nature (London) **457**, 301–304 (2009).
[53] R. P. J. Kunnen, B. J. Geurts, and H. J. H. Clercx, "Experimental and numerical investigation of turbulent convection in a rotating cylinder," J. Fluid Mech. **642**, 445–476 (2010).
[54] R. E. Ecke and J. J. Niemela, "Heat transport in the geostrophic regime of rotating Rayleigh-Bénard convection," preprint arXiv:1309.6672 (2013).
[55] F. Zhong, R. Ecke, and V. Steinberg, "Rotating Rayleigh–Bénard convection: Asymmetric modes and vortex states," J. Fluid Mech. **249**, 135–159 (1993).
[56] Y. Liu and R. E. Ecke, "Heat transport measurements in turbulent rotating Rayleigh-Bénard convection," Phys. Rev. E **80**, 036314 (2009).

[57] S. Schmitz and A. Tilgner, "Heat transport in rotating convection without Ekman layers," Phys. Rev. E **80**, 015305(R) (2009).
[58] S. Weiss and G. Ahlers, "Heat transport by turbulent rotating Rayleigh–Bénard convection and its dependence on the aspect ratio," J. Fluid Mech. **684**, 407–426 (2011).
[59] R. P. J. Kunnen, H. J. H. Clercx, and B. J. Geurts, "Heat flux intensification by vortical flow localization in rotating convection," Phys. Rev. E **74**, 056306 (2006).
[60] R. J. Stevens, H. J. Clercx, and D. Lohse, "Optimal Prandtl number for heat transfer in rotating Rayleigh–Bénard convection," New J. Phys. **12**, 075005 (2010).
[61] G. I. Taylor, "Experiments with rotating fluids," Proc. Roy. Soc. (London) **100**, 114–121 (1921).
[62] J. Proudman, "On the motion of solids in a liquid possessing vorticity," Proc. Roy. Soc. (London) A **92**, 408–424 (1916).
[63] S. Chandrasekhar, *Hydrodynamic and Hydromagnetic Stability* (Clarendon Press, Oxford, 1961).
[64] S. Schmitz and A. Tilgner, "Transitions in turbulent rotating Rayleigh-Bénard convection," Geophys. Astrophys. Fluid Dyn. **104**, 481–489 (2010).
[65] K. Petschel, S. Stellmach, M. Wilczek, J. Lülff, and U. Hansen, "Dissipation layers in Rayleigh-Bénard convection: A unifying view," Phys. Rev. Lett. **110**, 114502 (2013).
[66] A. Sameen, R. Verzicco, and K. Sreenivasan, "Non-Boussinesq convection at moderate Rayleigh numbers in low temperature gaseous helium," Phys. Scr. **2008**, 014053 (2008).